Research Article | Vol. 26, No. 10 | 14 May 2018 | OPTICS EXPRESS A374

Optics EXPRESS

Method to design a live coral cover sensitive index for multispectral satellite images

RONGYONG HUANG,[1,2,3] KEFU YU,[1,2,3,*] YINGHUI WANG,[1,2,3] WENHUAN WANG,[1,2,3] LIN MU,[4] AND JIKUN WANG[1,2,3]

[1]*Guangxi Laboratory on the Study of Coral Reefs in South China Sea, Guangxi University, Nanning 530004, China*
[2]*Coral Reef Research Centre of China, Guangxi University, Nanning 530004, China*
[3]*School of Marine Sciences, Guangxi University, Nanning 530004, China*
[4]*Institute of Complexity Science and Big Data Technology, Guangxi University, Nanning 530004, China*
**kefuyu@scsio.ac.cn*

Abstract: Live coral cover (LCC) is regarded as the most efficient indicator of coral reef health. However, LCCs are usually sampled with standardized transect or photo quadrat techniques in field, which are incomplete and labour-intensive. To overcome such difficulties, we study a model to transfer the pixels of multispectral satellite images to quantitative LCCs. The idea is to extend band ratio-based (BR) indices to a novel index constructed using the ratio of different linear combinations (RDLC) of band reflectance and water depths. On the basis of field surveyed LCCs, an empirical process is further proposed to solve the unknown parameters of this RDLC. This approach provides new thinking for designing LCC-sensitive indices for given multispectral satellite images. The experimental results on Weizhou Island and Palmyra Atoll demonstrate that the method is effective and feasible, where the mean relative errors (MREs) are improved from 45 to 56% for BRs to 23–29% for RDLCs for Weizhou Island.

OCIS codes: (280.0280) Remote sensing and sensors; (280.1415) Biological sensing and sensors.

References and links

1. J. H. Connell, "Diversity in tropical rain forests and coral reefs," Science **199**(4335), 1302–1310 (1978).
2. K. Yu, "Coral reefs in the South China Sea: Their response to and records on past environmental changes," Sci. China Earth Sci. **55**(8), 1217–1229 (2012).
3. D. R. Bellwood and T. P. Hughes, "Regional-scale assembly rules and biodiversity of coral reefs," Science **292**(5521), 1532–1535 (2001).
4. P. V. D. N. Araújo and R. Farias Do Amaral, "Mapping of coral reefs in the continental shelf of Brazilian Northeast through remote sensing," Revista de Gestão Costeira Integrada **16**(1), 5–20 (2016).
5. C. Wilkinson, *Status of Coral Reefs of the World* (Australian Institute of Marine Science, Townsville, 2004).
6. J. M. Pandolfi, R. H. Bradbury, E. Sala, T. P. Hughes, K. A. Bjorndal, R. G. Cooke, D. McArdle, L. McClenachan, M. J. H. Newman, G. Paredes, R. R. Warner, and J. B. C. Jackson, "Global trajectories of the long-term decline of coral reef ecosystems," Science **301**(5635), 955–958 (2003).
7. C. M. Newman, A. J. Knudby, and E. F. Ledrew, "Assessing the effect of management zonation on live coral cover using multi-date IKONOS satellite imagery," J. Appl. Remote Sens. **1**(1), 285–300 (2007).
8. S. English, C. Wilkinson, and V. Baker, *Survey manual for Tropical Marine Resources* (Australian Institute of Marine Science, 1997).
9. K. E. Joyce, S. R. Phinn, and C. M. Roelfsema, "Live Coral Cover Index Testing and Application with Hyperspectral Airborne Image Data," Remote Sens. (Basel) **5**(12), 6116–6137 (2013).
10. M. Zhao, K. Yu, Q. Shi, H. Yang, B. Riegl, Q. Zhang, H. Yan, T. Chen, G. Liu, and Z. Lin, "The coral communities of Yongle atoll: status, threats and conservation significance for coral reefs in South China Sea," Mar. Freshw. Res. **67**(12), 1888–1896 (2016).
11. K. E. Joyce and S. R. Phinn, "Spectral index development for mapping live coral cover," J. Appl. Remote Sens. **7**(1), 262–279 (2013).
12. M. A. Hamel and S. Andréfouët, "Using very high resolution remote sensing for the management of coral reef fisheries: Review and perspectives," Mar. Pollut. Bull. **60**(9), 1397–1405 (2010).
13. H. T. Kobryn, K. Wouters, L. E. Beckley, and T. Heege, "Ningaloo reef: shallow marine habitats mapped using a hyperspectral sensor," PLoS One **8**(7), e70105 (2013).

#319363 https://doi.org/10.1364/OE.26.00A374
Journal © 2018 Received 16 Jan 2018; revised 2 Mar 2018; accepted 3 Mar 2018; published 23 Mar 2018

Optics EXPRESS

14. S. R. Phinn and C. M. R. P. Mumby, "Multi-scale, object-based image analysis for mapping geomorphic and ecological zones on coral reefs," Int. J. Remote Sens. **33**(12), 3768–3797 (2012).
15. C. Roelfsema, S. Phinn, S. Jupiter, and J. C. S. Albert, "Mapping coral reefs at reef to reef-system scales, 10s-1000s km2, using object-based image analysis," nt. Yaogan Xuebao **34**, 6367–6388 (2013).
16. J. Leon and C. D. Woodroffe, "Improving the synoptic mapping of coral reef geomorphology using object-based image analysis," Int. J. Geogr. Inf. Sci. **25**(6), 949–969 (2011).
17. S. Hamylton, "Estimating the coverage of coral reef benthic communities from airborne hyperspectral remote sensing data: multiple discriminant function analysis and linear spectral unmixing," Int. J. Remote Sens. **32**(24), 9673–9690 (2011).
18. E. J. Hochberg and M. J. Atkinson, "Capabilities of remote sensors to classify coral, algae, and sand as pure and mixed spectra," Remote Sens. Environ. **85**(2), 174–189 (2003).
19. H. Holden and E. Ledrew, "Hyperspectral identification of coral reef features," Int. J. Remote Sens. **20**(13), 2545–2563 (1999).
20. J. D. Hedley, C. M. Roelfsema, S. R. Phinn, and P. J. Mumby, "Environmental and Sensor Limitations in Optical Remote Sensing of Coral Reefs: Implications for Monitoring and Sensor Design," Remote Sens. (Basel) **4**(12), 271–302 (2012).
21. C. Yun and D. Gillieson, "Evaluation of Landsat TM vegetation indices for estimating vegetation cover on semi-arid rangelands: a case study from Australia," Can. J. Rem. Sens. **35**, 435–446 (2014).
22. A. C. Xavier and C. A. Vettorazzi, "Mapping leaf area index through spectral vegetation indices in a subtropical watershed," Int. J. Remote Sens. **25**(9), 1661–1672 (2004).
23. P. J. Mumby, J. D. Hedley, J. Chisholm, C. D. Clark, H. Ripley, and J. Jaubert, "The cover of living and dead corals from airborne remote sensing," Coral Reefs **23**(2), 171–183 (2004).
24. K. E. Joyce, "A method for mapping live coral cover using remote sensing," PhD Thesis, University of Queensland (2005).
25. A. Minghelli-Roman, J. R. Chisholm, M. Marchioretti, and J. M. Jaubert, "Discrimination of coral reflectance spectra in the Red Sea," Coral Reefs **21**(3), 307–314 (2002).
26. A. Collin, J. L. Hench, and S. Planes, "A novel spaceborne proxy for mapping coral cover," in *Proceedings of the 12th International Coral Reef Symposium* (Cairns, Australia, 2012).
27. P. J. Mumby, E. P. Green, A. J. Edwards, and C. D. Clark, "Coral reef habitat mapping: how much detail can remote sensing provide?" Mar. Biol. **130**(2), 193–202 (1997).
28. K. Yu and J. Zhao, "Coral reefs (of the South China Sea)," in *The South China Sea – Paleoceanography and Sedimentology*, P. Wang, and Q. Li, eds. (Springer, 2009), pp. 229–248.
29. T. Chen, S. Li, K. Yu, Z. Zheng, L. Wang, and T. Chen, "Increasing temperature anomalies reduce coral growth in the Weizhou Island, northern South China Sea," Estuar. Coast. Shelf Sci. **130**, 121–126 (2013).
30. T. Chen, Z. Zheng, S. Mo, C. Tang, and X. Zhou, "Bioerosion in Porites corals at Weizhou Island and its environmental significance," Chin. Sci. Bull. **58**(17), 1574–1582 (2013).
31. W. Wang, K. Yu, and Y. Wang, "A Review on the Research of Coral Reefs in the Weizhou Island,Beibu Gulf," Trop. Geogr. **36**, 72–79 (2016).
32. L. I. Deren and W. Mi, "On-orbit Geometric Calibration and Accuracy Assessment of ZY-3," Spacecraft Recovery Remote Sensing **33**, 1–6 (2012).
33. L. Li, H. Luo, and H. Zhu, "Estimation of the Image Interpretability of ZY-3 Sensor Corrected Panchromatic Nadir Data," Remote Sens. (Basel) **6**(12), 4409–4429 (2014).
34. X. Wen, G. Shule, L. Xiaoxiang, W. Xiaoyan, and L. Junjie, "Radiometric Image Quality Assessment of ZY-3 TLC Camera," Spacecraft Recovery & Remote Sensing (2012).
35. R. Huang, K. Yu, Y. Wang, J. Wang, L. Mu, and W. Wang, "Bathymetry of the Coral Reefs of Weizhou Island Based on Multispectral Satellite Images," Remote Sens. (Basel) **9**(12), 750 (2017).
36. L. Li, H. Luo, X. Tang, and Z. Li, "Characteristic analysis and quality assessment of ZY-3 multi-spectral image," Remote sensing for land and resources **26**, 17–24 (2014).
37. N. W. Longbotham, F. Pacifici, S. Malitz, W. Baugh, and G. Campsvalls, "Measuring the Spatial and Spectral Performance of WorldView-3," in *Hyperspectral Imaging and Sounding of the Environment 2015* (Lake Arrowhead, California United States, 2015).
38. Q. Tian, L. Zheng, and Q. Tong, "Image based atmospheric radiation correction and reflectance retrieval methods," Quarterly J. Appl. Meteorology **9**, 456–461 (1998).
39. G. Doxani, M. Papadopoulou, P. Lafazani, C. Pikridas, and M. Tsakiristrati, "Shallow-Water Bathymetry Over Variable Bottom Types Using Multispectral WORLDVIEW-2 Image," ISPRS - International Archives of the Photogrammetry, Remote Sensing and Spatial Information Sciences XXXIX **B8**, 159–164 (2012).
40. D. R. Lyzenga, N. P. Malinas, and F. J. Tanis, "Multispectral bathymetry using a simple physically based algorithm," IEEE Trans. Geosci. Remote Sens. **44**(8), 2251–2259 (2006).
41. H. Mohamed, A. Negm, M. Zahran, and O. C. Saavedra, "Bathymetry Determination from High Resolution Satellite Imagery Using Ensemble Learning Algorithms in Shallow Lakes," Case Study El-Burullus Lake **7**, 295–301 (2016).
42. O. Yuzugullu and A. Aksoy, "Generation of the bathymetry of a eutrophic shallow lake using WorldView-2 imagery," J. Hydroinform. **16**(1), 50–59 (2014).

Optics EXPRESS

43. M. Papadopoulou, P. Lafazani, E. R. Mavridou, M. Tsakiri-Strati, and G. Doxani, "Creation of Digital Bathymetric Maps using High Resolution Satellite Imagery and Multispectral Bathymetric Modeling for Shallow Waters," Tour. Manage. **14**, 407–408 (2015).
44. Z. Lee, K. L. Carder, C. D. Mobley, R. G. Steward, and J. S. Patch, "Hyperspectral remote sensing for shallow waters. I. A semianalytical model," Appl. Opt. **37**(27), 6329–6338 (1998).
45. F. Eugenio, J. Marcello, and J. Martin, "High-Resolution Maps of Bathymetry and Benthic Habitats in Shallow-Water Environments Using Multispectral Remote Sensing Imagery," IEEE Trans. Geosci. Remote Sens. **53**(7), 3539–3549 (2015).
46. Z. Lee, K. L. Carder, C. D. Mobley, R. G. Steward, and J. S. Patch, "Hyperspectral remote sensing for shallow waters. 2. Deriving bottom depths and water properties by optimization," Appl. Opt. **38**(18), 3831–3843 (1999).
47. Z. Lee, K. L. Carder, R. F. Chen, and T. G. Peacock, "Properties of the water column and bottom derived from Airborne Visible Infrared Imaging Spectrometer (AVIRIS) data," J. Geophys. Res. **106**(C6), 11639–11652 (2001).
48. P. N. Bierwirth, "Shallow sea-floor reflectance and water depth derived by unmixing multispectral imagery," Photogramm. Eng. Remote Sensing **59**, 331–338 (1993).
49. D. R. Lyzenga, "Passive remote sensing techniques for mapping water depth and bottom features," Appl. Opt. **17**(3), 379–383 (1978).
50. L. Hu, Z. Liu, Z. Liu, C. Hu, and M. X. He, "Mapping bottom depth and albedo in coastal waters of the South China Sea islands and reefs using Landsat TM and ETM+ data," Int. J. Remote Sens. **35**(11-12), 4156–4172 (2014).
51. S. D. Jawak and A. J. Luis, "High-resolution multispectral satellite imagery for extracting bathymetric information of Antarctic shallow lakes," Proceedings of SPIE - The International Society for Optical Engineering (2016).
52. S. Maritorena, A. Morel, and B. Gentili, "Diffuse reflectance of oceanic shallow waters: Influence of water depth and bottom albedo," Limnol. Oceanogr. **39**(7), 1689–1703 (1994).
53. M. L. Zoffoli, R. Frouin, and M. Kampel, "Water Column Correction for Coral Reef Studies by Remote Sensing," Sensors (Basel) **14**(9), 16881–16931 (2014).
54. S. Khanna, M. J. Santos, S. L. Ustin, K. Shapiro, P. J. Haverkamp, and M. Lay, "Comparing the potential of multispectral and hyperspectral data for monitoring oil spill impact," Sensors (Basel) **18**(2), 558 (2018).
55. R. V. Platt and A. F. H. Goetz, "A Comparison of AVIRIS and Landsat for Land Use Classification at the Urban Fringe," Photogramm. Eng. Remote Sensing **70**(7), 813–819 (2004).
56. M. Zhao, K. Yu, Q. Zhang, and Q. Shi, "Long-term change in coral cover in luhuitou fringing reef, Sanya," Oceanol. Limnol. Sin. **41**, 440–447 (2010).
57. Q. Zhang, Q. Shi, G. Chen, T. C. W. Fong, D. C. C. Wong, H. Huang, H. Wang, and M. Zhao, "Status monitoring and health assessment of Luhuitou fringing reef of Sanya, Hainan, China," Chin. Sci. Bull. **51**(S2), 81–88 (2006).
58. F. Eugenio, J. Martin, J. Marcello, and E. Fraile-Nuez, "Environmental monitoring of El Hierro Island submarine volcano, by combining low and high resolution satellite imagery," Int. J. Appl. Earth Obs. Geoinf. **29**, 53–66 (2014).

1. Introduction

Coral reefs are considered to be marine ecosystems containing the highest level of biodiversity and primary productivity, and they are comparable with tropical rainforests on land [1–4]. They can protect coastlines, provide natural habitat for sea creatures, and act as tourism and fishery resources for humans [2]. Thus, they are very important to the healthy and sustainable development of future human society and the marine ecological environment. However, as biodiversity hotspots of the oceans, coral reefs have long been in decline worldwide [5] because of anthropogenic destruction and global change, including global warming and oceanic acidification [6]. All of these result in a rapid decrease in the coverage rate of living corals [7], and thus, live coral cover (LCC) is regarded as the best measure of coral reef health [2]. Therefore, the estimation of LCC is an important part of the research, conservation and management of current coral reefs.

Unfortunately, LCC is usually assessed in field surveys using standardized transect or photo quadrat techniques [8–10]. These in-field methods are labour-intensive, time-consuming and costly. Especially, they are suitable only for surveying a few typical transects or points rather than the whole area of the coral reefs. Therefore, repetitive in-field surveying of LCCs may be impractical and unfeasible, particularly for a large area of coral reefs. Remote sensing is regarded as a great potential way to increase this coverage [11], and for this reason, many studies have focused on exploring the potential of optical remote sensing images on the LCC estimation.

Optics EXPRESS

Classification of remote sensing images is considered an intuitive and low-cost way to estimate the distribution of live corals over large clear-water areas, so it is usually regarded as an excellent tool for guiding strategy for sampling and identifying conservation areas [4, 12]. Kobryn et al. [13] made use of a set of airborne hyperspectral data to classify the habitat categories of the clear-water Ningaloo Reef. The results show that the overall accuracy is approximately 70% for the highest classification level (including 46 classes of abiotic and biotic seabed components and hard coral growth forms). To improve the accuracy, the state-of-the-art object-based image analysis (OBIA) has been introduced into the image classification of coral reefs [14–16]. The overall accuracy of 'benthic community' classifications reaches 52% to 75% for 2.4 m resolution Quickbird-2 and 4.0 m resolution IKONOS satellite images [14, 15]. Nevertheless, we should note that the accuracy is usually practical for high-resolution hyperspectral image data but may be far from acceptable for multispectral satellite images. Hamel and Andréfouët [12] demonstrated that few utilizations of multispectral satellite images were reported in habitat mapping. They thought this was likely because of inherent technology limitations and lack of awareness of the possibilities.

LCCs can be simply estimated by counting the ratio of the live coral pixels from the habitat mapping. However, as any one of the pixels may consist of several different habitat categories, classifications for habitat mapping are actually not equivalent to LCC estimation. This problem is now even worse because of the long-term decline of coral reefs. Therefore, LCCs may be underestimated by just counting from the classifications. Such problems have been identified in the past and have been regarded as a significant challenge for coral reef mapping [17–20].

To improve the detection of the LCCs, one idea is to make use of image transforms or indices that are extended from the vegetation indices [21, 22] for biophysical information extraction in terrestrial environments. Mumby et al. [23] used the spectral derivatives of airborne hyperspectral images to map various stages of coral mortality. Joyce et al. [9, 11, 24] described the development and application of several spectral indices for LCC mapping, which is in the form of reflectance, derivatives, and the band ratios of airborne hyperspectral images. The results demonstrate that the second derivative of the reflectance at 564 nm was one of the most sensitive to the variation in LCCs and least sensitive to the variation in water depth. They also noted that a simple band ratio (SBR) of 529:439 nm showed the greatest sensitivity to LCC variation around clear-water reefs. Minghelli-Roman et al. [25] also tried to utilize band ratio (BR) indices to discriminate different coral genera according to field spectrometry. Collin et al. [26] tried to test the viability of band ratio indices for a WorldView-2 image recently and found that the normalized difference ratio (NDR) of green-purple bands reached the highest positive correlation with the in-field LCC.

The confounding influence of variable depths on bottom reflectance is regarded as one of the most common difficulties with remote sensing of underwater environments [27]. However, most of the studies demonstrated that band ratio- and derivative-based methods stated a requirement for clear water and that substrate discrimination will decrease as the water depth increases [9]. Moreover, we should note that most conclusions from band ratio- and derivative-based indices were tested on airborne hyperspectral images, field spectrometer data, or simulated mixtures of benthic feature types [11]. Due to the assumption of linear mixing, the inadequate characterization of representative pure pixels, the lack of consideration for water column effects, etc., those results from the airborne hyperspectral image and field spectrometer would be different from multispectral satellite images [9]. For example, it is difficult to calculate second derivatives and band ratios that are exactly the same as the ones recommended by the experiments of the airborne hyperspectral images and the field spectrometer data. In fact, to calculate the band ratios with multispectral images, one need to select the bands that are closest to the ones recommended by hyperspectral data. Moreover, those bands of multispectral images are usually much broader than those of hyperspectral data.

In this study, we focus on extending SBR and NDR to a more general index using the ratio of different linear combinations (RDLC) of the band reflectance and the water depths for LCC estimation. Although the direct motive was to improve the accuracy of the LCCs estimated by multispectral satellite images in our study area, we actually provides a new way to design methods for LCC estimation. We wish for it to help exploit the potential of multispectral satellite remote sensing for estimating LCCs of coral reefs.

2. Materials and methods

2.1 Materials

To test the proposed RDLC, the coral fringing reefs around Weizhou Island (21°00′-21°05′ N, 109°00′-109°10′ E) in the Beibu Gulf, northern South China Sea were chosen as our main study area, as shown in Fig. 1. Coral reefs have been developing around Weizhou Island since the mid-Holocene, and these reefs cover an area of approximately 6–8 km^2 [2, 28]. These coral reefs have long been the focus of studies analysing the response of coral to global warming and human disturbance, because they are located in a relatively high-latitude area and are heavily influenced by anthropogenic activity [28–31].

According to Wang et al. [31], the annual average Sea Surface Temperature (SST) and salinity values around Weizhou Island are approximately 24.55 °C and 31.9‰ respectively, thus it is ideal for coral growth even though the seawater transparency varies only from 3.0 m to 10.0 m [31]. However, the live corals around Weizhou Island have been declining over the last decades [31]: the average of the LCCs around Weizhou Island has been reduced from 69.28 (1991) to 16.21 (2010). Note that LCCs are all signed by a number range from 0 to 100 in this paper for convenience; e.g., LCC expressed by 25 means 25%.

Optics EXPRESS

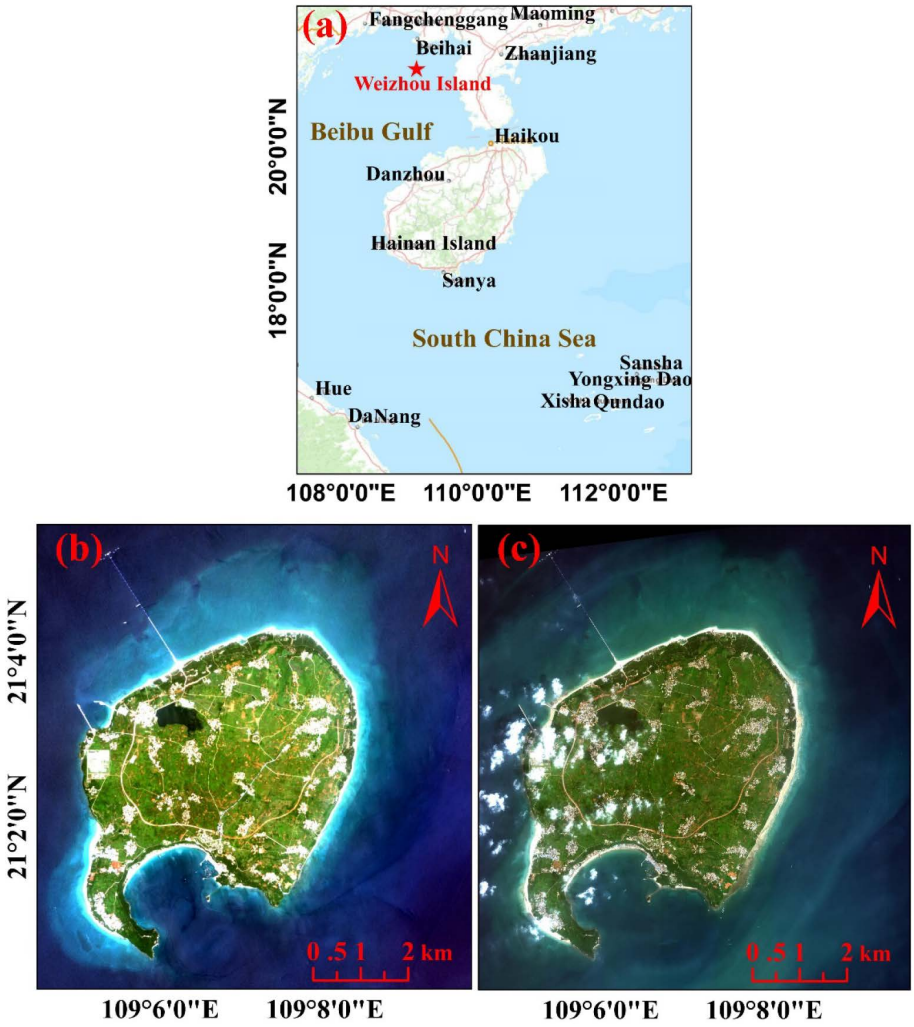

Fig. 1. The position of Weizhou Island and the corresponding experimental satellite images: (a) position of Weizhou Island (the pentagram); (b) ZY-3 image; and (c) WV-3 image.

The experimental images of Weizhou Island consist of one ZY-3 multispectral image and one WorldView-3 (WV-3) multispectral image, as shown in Fig. 1. The main purpose of applying these two different images to Weizhou Island is to verify the proposed RDLC method is effective and feasible for different multispectral images, and test its improvement comparing with the SBR and NDR methods.

The ZY-3 satellite was launched on January 9, 2012 as the first civil high-resolution optical transmission surveying and mapping satellite of China. The ZY-3 multispectral image chosen as one of the remote sensing data sources for the experiments was acquired by the nadir multispectral camera of the ZY-3 satellite on August 24, 2015. It consists of 4 different wave bands (Blue, Green, Red, and Near-IR). The image is geo-referenced in the world geodetic system (WGS-84) with a ground resolution of 5.8 m. The geo-positioning accuracy is higher than 14.0 m without ground control after undergoing the on-orbit geometric

calibration [32]. The signal-to-noise ratios (SNR) was reported to range approximately from 40—50 [33–35] for some typical signal radiances. More about the radiometric image quality of the ZY-3 multispectral image can be referenced to the result of Li et al. [36].

The WV-3 satellite was launched by Digital Globe Inc., Longmont, CO, USA on August 13, 2014. It provides panchromatic, multispectral, shortwave infrared, and CAVIS images with resolutions of 0.31 m, 1.24 m, 3.7 m, and 30 m, respectively. The WV-3 multispectral image used in our experiments was acquired on October 1, 2015. The geo-positioning accuracy is predicted to be higher than 3.5 m CE90 without ground control [37]. The WV-3 multispectral images consist of 8 different wave bands (Coastal, Blue, Green, Yellow, Red, RedEdge, Near-IR1, and Near-IR2). As can be seen in Fig. 1, the southern, southwestern, and western areas of the WV-3 image are seriously influenced by clouds, therefore, we can study only the northwestern, northern, northeastern, eastern, and southeastern regions of the image in our experiments.

Field surveyed LCCs around Weizhou Island were investigated in October 2015 along thirteen 100-m transects, and matched to the satellite data by using the geo-referenced information, as shown in Appendix A.

Note that, the subsurface remote sensing reflectance needs to be first extracted from the experimental images before study of the LCC estimation. The purpose is to eliminate the influence of the sunglint, atmospheric absorption and scattering of the solar radiation, i.e., make sure that the extracted subsurface remote sensing reflectance images contain only the signals of the water column and the bottom reflectance. As this preprocessing is not the focus of this study, we just simply make use of the approach developed by Huang et al. [35] for extracting the subsurface remote sensing reflectance. The approach mainly consists of the following subapproaches: radiometric calibration, atmospheric correction (using both the tropical atmospheric model and maritime aerosols model in the Second Simulation of a Satellite Signal in the Solar Spectrum (6S) radiative transfer code), sunglint correction, and subsurface remote sensing reflectance estimation. According to the experiments of Tian et al. [38], the precision of this atmospheric correction approach is about 6%. For convenience, we sign the subsurface remote sensing reflectance as ρ in all the next sections.

Besides, we found that benthic habitats of the northern Pacific Palmyra Atoll (as shown in Fig. 2) have been mapped by National Centers for Coastal Ocean Science (NCCOS) during January 2009 and December 2011 (https://coastalscience.noaa.gov/project/benthic-habitat-mapping-palmyra-atoll/). Palmyra Atoll is located roughly halfway between Hawaii and American Samoa, and its reefs are some of the most pristine anywhere in the world. To take another validation site, we further use this habitat map to expand the proposed RDLC to Palmyra Atoll in the experiments.

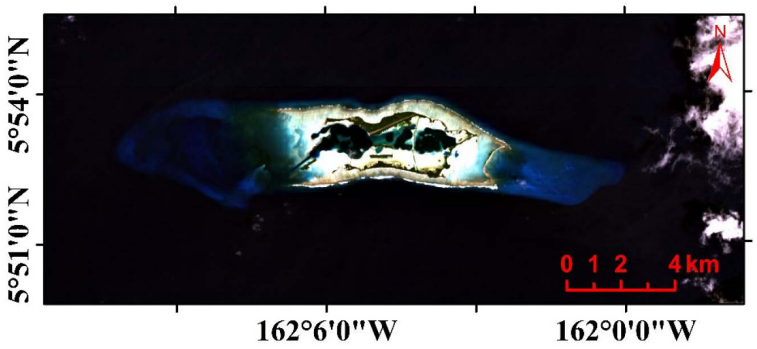

Fig. 2. The EO-1 ALI multispectral image of the northern Pacific Palmyra Atoll.

The experimental image of Palmyra Atoll is captured by Advanced Land Imager (ALI) of the Earth Observing-1 (EO-1) mission on October 18, 2009. EO-1 ALI is part of NASA's New Millennium Program (NMP) and has validated a multispectral instrument that is a significant improvement over the Landsat 7 ETM + instrument. The experimental ALI multispectral image consists of 9 different wave bands (Coastal, Blue, Green, Red and 5 Infrared bands) with a ground resolution of 30 m. On the other hand, ALI was used to validate and demonstrate technology for the Landsat Data Continuity Mission (LDCM), i.e. the operational land imager (OLI) on Landsat 8 (http://eo1.usgs.gov), so the ALI image shares similar resolution and wave bands with OLI. As a result, except for a second validation site, another purpose of applying the ALI image is to test the effectiveness and feasibility on some other freely available images, such as ALI or OLI. As the ZY-3 and WV-3 images, the subsurface remote sensing reflectance of the ALI multispectral image is also extracted by using the approach developed by Huang et al. [35] before the experiments.

The difference between the Weizhou Island data and the Palmyra Atoll data is that LCCs around Weizhou Island are all continuous values (see Appendix A), while LCCs provided by NCCOS is four live coral density classes (0–10, 10–50, 50–90, and 90–100).

2.2 Methods

In this section, the radiative transfer model of the water column is described in brief followed by methods to extend SBR (or NDR) to RDLC for the LCC estimation in multispectral satellite images. The main idea comes from the following two aspects: (1) based on previous studies on hyperspectral data, LCCs should correlate linearly to a particular SBR (or NDR); (2) according to the principle of band combination bathymetric methods [39–43], there is an approximate linear dependence between the water depth and the combination of different bands.

2.2.1 Radiative transfer model of the water column

An accurate and typical radiative water column transfer model was developed by Lee et al. [44] and was applied to semi-analytic map methods for bathymetry and benthic habitats [35, 45, 46]. For this radiative transfer model, the optical path-elongation factors for scattered photons from the water column and the bottom, the diffuse attenuation coefficient, and the subsurface remote-sensing reflectance for optically deep waters can be parameterized by using the chlorophyll-a, the colored dissolved organic matter (CDOM, also called gelbstoff or yellow substance), and the effective backscattering coefficient for particles [44, 46, 47]. The error of the subsurface remote-sensing reflectance simulated by using the model can reach approximately 3% [44], but the corresponding method for water property estimation was originally designed for hyperspectral data [46, 47] and may be difficult to implement for multispectral imagery. What is more, this radiative transfer model is more complicated than those of Bierwirth [48] and Lyzenga et al. [40, 49], which are based on the law that light is attenuated exponentially with depth in the water column. As a result, many current studies [43, 50–53] chose Bierwirth or Lyzenga's model rather than the more accurate one proposed by Lee et al. [44] as the beginning and the foundation of their research.

Similarly, we start our studies from the radiative transfer model applied by Lyzenga et al. [40, 49] for simplicity as follows:

$$L(\lambda) = L_{\infty}(\lambda) + k(\lambda)\rho_b(\lambda)\exp\left[-\kappa(\lambda) fH\right] \tag{1}$$

where L is the subsurface radiance emerging from the water mass containing the reflective signals from the substrate and the water column; L_{∞} is the subsurface radiance for optically deep water; k is a constant that includes the solar irradiance, the transmittance of the atmosphere and the water surface, and the reduction of the radiance due to refraction at the water surface; ρ_b is the substrate radiance reflectance, which can also be expressed as

substrate irradiance reflectance divided by π ; f is a geometric factor accounting for the path-length through the water, H is the water depth, and κ is the effective diffuse attenuation coefficient of the water column.

When Eq. (1) is divided by the downwelling irradiance just below the water surface E_{d0^-}, we can obtain

$$\rho(\lambda) = \rho_\infty(\lambda) + t(\lambda)\rho_b(\lambda)\exp\left[-\kappa(\lambda) fH\right] \tag{2}$$

i.e.

$$\rho(\lambda) - \rho_\infty(\lambda) = t(\lambda)\rho_b(\lambda)\exp\left[-\kappa(\lambda) fH\right] \tag{3}$$

where ρ is the subsurface remote sensing reflectance, ρ_∞ is the subsurface remote-sensing reflectance for optically deep water, and t is a constant that is equal to k divided by E_{d0^-}.

2.2.2 Construction of the RDLC for LCC estimation

Taking the logarithm of both sides, Eq. (3) can be then rewritten as

$$\ln\left[\rho(\lambda) - \rho_\infty(\lambda)\right] = \ln t(\lambda) + \ln \rho_b(\lambda) - \kappa(\lambda) fH \tag{4}$$

As previously shown in aspect (2), there is an approximately linear dependence between the water depth and the combination of different bands. More specifically,

$$\sum\nolimits_i a_i \ln\left[\rho(\lambda_i) - \rho_\infty(\lambda_i)\right] = \sum\nolimits_i a_i t(\lambda_i) + \sum\nolimits_i a_i \ln \rho_b(\lambda_i) - 2f\sum\nolimits_i a_i \kappa(\lambda_i) H \tag{5}$$

where $i = 1, 2, 3, \ldots$ indicate different wave bands.

If the coefficient of H is not equal to zero, Eq. (5) can be seen as the bathymetric model of band combination. However, we take Eq. (5) from a different angle in this study as follows: it is able to construct a series of indices through selecting different a_i as

$$I(a_i) = \sum\nolimits_i a_i \ln \rho_b(\lambda_i) = \sum\nolimits_i a_i \ln\left[\rho(\lambda_i) - \rho_\infty(\lambda_i)\right] - \sum\nolimits_i a_i t(\lambda_i) + 2f\sum\nolimits_i a_i \kappa(\lambda_i) H \tag{6}$$

The middle of Eq. (6) shows that $I(a_i)$ depends only on the substrate radiance reflectance, whereas the right illustrates that $I(a_i)$ can be calculated by using the linear combination of the water depth and the subsurface remote sensing reflectance of different bands.

As previously shown in aspect (1), LCCs should be linearly correlated with particular SBR (or NDR) for hyperspectral data. However, for multispectral satellite images, it is hard to calculate the SBR (or NDR) that is exactly the same as the one derived from hyperspectral data, because none of the multispectral satellite sensors is now designed according to such SBR (or NDR). We can only select two similar broad bands from the multispectral images to approximate the SBR (or NDR) in practice. As a result, LCCs estimated by such SBR and NDR were found to be less accurate in our study area (see the experiments).

Inspired by the idea of SBR (or NDR), we plan to extend SBR (or NDR) to another index expressed by the RDLC of the substrate band reflectance for the LCC estimation. However, if the linear combinations of the subsurface remote sensing reflectance are utilized to construct the index directly, we find it is difficult to separate the water depth from the subsurface remote sensing reflectance according to Eq. (2). As a result, we decide to utilize $I(a_i)$ expressed by Eq. (6) to construct the RDLC as

$$I(a_i, a_i') = \frac{I(a_i)}{I(a_i')} = \frac{\sum_i a_i \ln \rho_b(\lambda_i)}{\sum_i a_i' \ln \rho_b(\lambda_i)} \tag{7}$$

and this is required to correlate with LCC as close as possible so that LCCs can be estimated by the following linear equation:

$$LCC = mI(a_i, a_i') + n \tag{8}$$

where m and n are constant coefficients. Thus a method is needed to determine the optimal a_i and a_i' to make the correlation coefficient between $I(a_i, a_i')$ and the LCC become maximum. The method for solving this problem is proposed in the following sub-section.

2.2.3 Implementation of the RDLC for LCC estimation

To determine the optimal a_i and a_i' and provide an approach to calculate $I(a_i, a_i')$, we note that Eq. (7) can be rewritten as follows according to Eq. (6):

$$I(a_i, a_i', b, b', c, c') = \frac{\sum_i a_i \ln\left[\rho(\lambda_i) - \rho_\infty(\lambda_i)\right] + bH + c}{\sum_i a_i' \ln\left[\rho(\lambda_i) - \rho_\infty(\lambda_i)\right] + b'H + c'} \tag{9}$$

where

$$\begin{cases} b = 2f\sum_i a_i \kappa(\lambda_i) \\ b' = 2f\sum_i a_i' \kappa(\lambda_i) \\ c = -\sum_i a_i t(\lambda_i) \\ c' = -\sum_i a_i' t(\lambda_i) \end{cases} \tag{10}$$

As shown in Eq. (7), a_i and a_i' are defined as the coefficients of the substrate radiance reflectance, and so are independent of the water depth and column properties. On the other hand, according to Eq. (10), b and b' depend on the effective diffuse attenuation coefficient of the water column and the geometric factor of the path-length through the water, c and c' are dependent on the solar irradiance, the transmittance of the atmosphere and the water surface, and the reduction of the radiance due to refraction at the water surface.

The advantage of Eq. (9) is that we can calculate the index using the subsurface remote sensing reflectance directly, whereas the problem is that it needs to estimate the water depth before the calculation. Fortunately, many studies [35, 40, 43, 45, 48–51] have developed methods to estimate water depth from multispectral images. Hence we can just suppose that the water depth was known, i.e., the water depths are estimated from the ZY-3 image by using the approach proposed by Huang et al. [35] in this study. The statistics are checked by comparing with 45 different measured depths: the maximum value of the absolute errors (MAX) is 2.27 m, the mean of the absolute errors (MAE) is 0.81 m, and the root mean square error (RMSE) is 1.01 m.

On the other hand, $\rho_\infty(\lambda_i)$ can be assumed to remain constant over the scene [48]. Thus, it is estimated using the minimum of the subsurface remote-sensing reflectance of the adjacent optically deep waters [45, 50].

To simplify the calculation, we follow the pattern of empirical band combination bathymetric methods [39–43] to see a_i, a_i', b, b', c, and c' as independent variants of $I(a_i, a_i', b, b', c, c')$. As $I(a_i, a_i', b, b', c, c')$ does not change when the numerator and the denominator are scaled by any non-zero real number at the same time, so we add the following two conditions:

$$\begin{cases} \sum_i a_i^2 = 1 \\ \sum_i a_i'^2 = 1 \end{cases} \tag{11}$$

As a result, the problem can now be described as follows: search a set of optimal a_i, a_i', b, b', c, and c' subject to Eq. (11) so that the correlation coefficient between the field LCC data and $I(a_i, a_i', b, b', c, c')$ becomes maximum. In this study, the Genetic Algorithm (GA) tool of Matlab 2012b software is used for solving this problem directly; the GA is well known as an optimization tool inspired by the process of natural selection in computer science.

Specifically, for a set of unknowns (a_i, a_i', b, b', c, and c'), half of the field LCCs obtained by sub-section 2.2.2 and their corresponding water depth H and subsurface remote sensing reflectance $\rho(\lambda_i)$ are seen as known data. H and $\rho(\lambda_i)$ are first substituted into Eq. (9) for obtaining a series of $I(a_i, a_i', b, b', c, c')$,and then the negative of the correlation coefficient is calculated as the GA fitness value between the LCCs and $I(a_i, a_i', b, b', c, c')$.

Once the GA finds the optimal a_i, a_i', b, b', c, and c' to let the fitness value reach minimum (which is equivalent to finding the maximum of the correlation coefficients), we further estimate m and n of Eq. (8) by regressing $I(a_i, a_i', b, b', c, c')$ against the field LCCs.

Thereafter, another half of the field LCC data can be used for accessing the accuracy. The approach is to estimate the LCCs from $\rho(\lambda_i)$ and H according to Eqs. (8) and (9), and then compare the results with the field LCCs.

Now, the implementation can be summarized and reviewed as shown in Fig. 3.

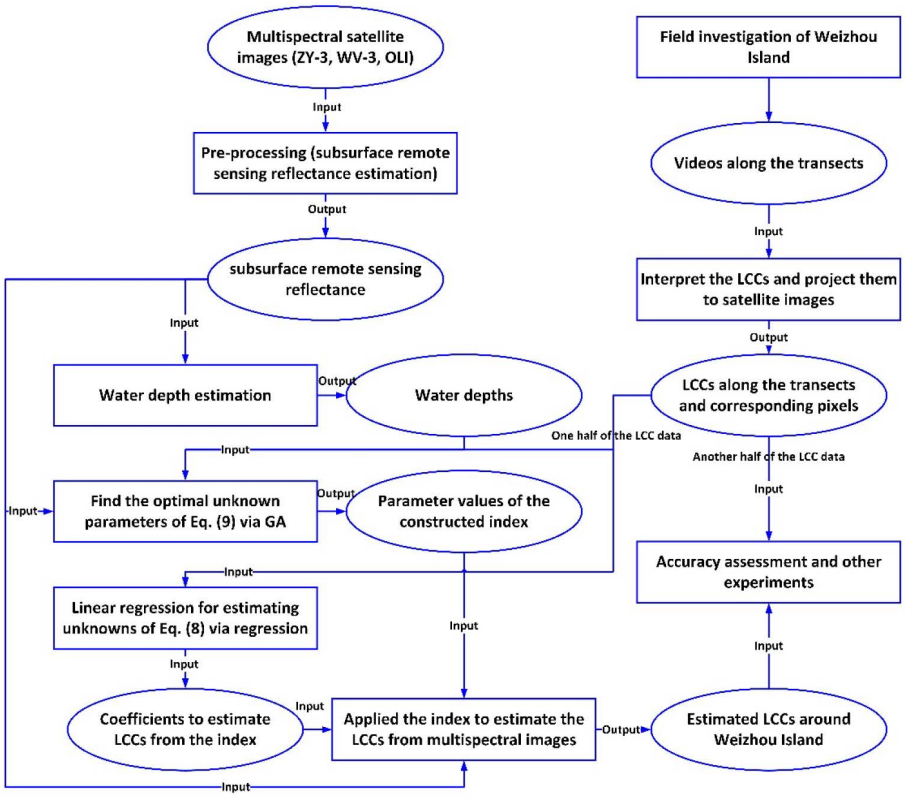

Fig. 3. The implementation of the RDLC model for estimating the LCCs of Weizhou Island.

However, when the Palmyra Atoll data is used, it is impossible to calculate the correlation coefficient, as the LCCs around Palmyra Atoll are provided with only four live coral density

classes. So we need to design a metric to measure the errors between the live coral density classes and the LCCs estimated by using Eq. (8) with $I(a_i, a_i', b, b', c, c')$.

If specific $\rho(\lambda_i)$ and H are corresponding to a live coral density class where the LCC range from u to v, we define the error between the live coral density class and the corresponding estimated LCC as follows:

$$E_{\rho,H}(a_i, a_i', b, b', c, c', m, n) = T(L_{\rho,H} < u)(u - L_{\rho,H}) + T(L_{\rho,H} > v)(L_{\rho,H} - v) \quad (12)$$

where $\mathrm{T}(\bullet) = 1$ if $\bullet$ is true, otherwise $\mathrm{T}(\bullet) = 1$, and

$$L_{\rho,H} = mI(a_i, a_i', b, b', c, c') + n \quad (13)$$

Equation (12) means that if the LCC estimated by substituting $\rho(\lambda_i)$ and H into Eq. (8) drops into the range of u to v, then the error is defined as zero, otherwise the error is the defined by the distance to the extreme points of the range. As a result, the objective function can be then defined as the mean of those errors:

$$E(a_i, a_i', b, b', c, c', m, n) = \frac{1}{N}\sum\nolimits_{\rho,H} E_{\rho,H}(a_i, a_i', b, b', c, c', m, n) \quad (14)$$

where N is the number of the errors.

Similar to the Weizhou Island data, GA is also used to search the optimal parameters by minimize the objective function for the Palmyra Atoll data. Specifically, 5600 points were randomly selected from the Palmyra Atoll data: one half is used to train the parameters, while the other half is used to verify the effectiveness. In other words, we need only to make use of objective function (14) instead of the negative of the correlation coefficient to search the optimal parameters for the Palmyra Atoll data.

Note that the proposed approach is different from other studies on indices derived from hyperspectral data: studies on indices derived from hyperspectral data are to select the optimal wave bands for a few given index forms, but the proposed approach is mainly to design an index for several given wave bands and provide a method to search the optimal parameters of the index for the LCC estimation.

3. Experimental results and analyses

In the experiments, we study on estimation the LCCs around Weizhou Island and Palmyra Atoll with the methods described in section 2.3. As most multispectral satellite images contain the blue, green, and red wavebands, we utilize only the blue, green, and red wavebands of the multispectral images through the calculation of the RDLC. The main experimental results and analyses are as follows.

3.1 Selection of the radius for field LCC calculation for Weizhou Island

For those transects of Weizhou Island (see Appendix A), the proper radius should be determined to fit the resolution of the multispectral images. To study this, we change the radius in the range of 2 m to 40 m for the field LCC measurement, and then we search the corresponding optimal parameters (a_i, a_i', b, b', c, and c') of the RDLC index described by Eq. (9), and regress the coefficients (m and n) of Eq. (8), using the proposed methods described in section 2.3. The correlation coefficients against these radii are shown in Fig. 4. We can see from the figure that the correlation coefficients of the ZY-3 and WV-3 images increase with the radius, but the increments of the correlation coefficients become very low once the radii reach approximately 25 m.

Optics EXPRESS

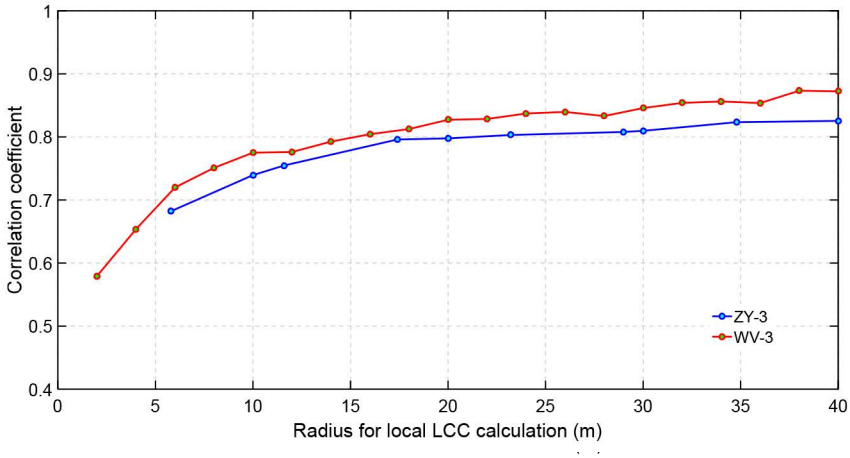

Fig. 4. The correlation coefficients of the constructed RDLCs against different radii for the experimental multispectral images.

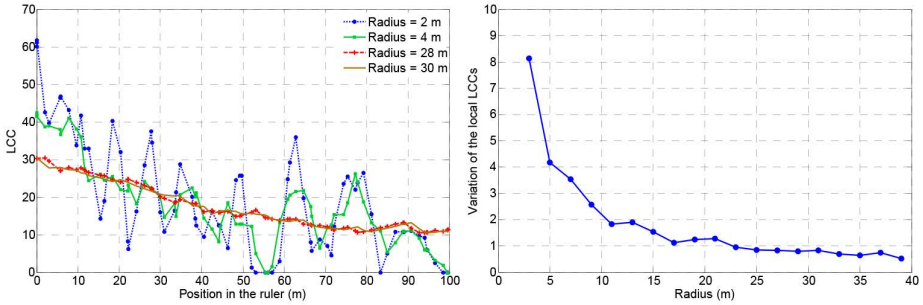

Fig. 5. The influence on the field surveyed local LCCs against different radii for a specific transect: (left) field surveyed local LCCs along the transect, which are calculated using different radii; (right) variations of field surveyed local LCCs along the transect against different radii.

On the other hand, according to Appendix A, the field measurement is actually estimating the LCCs with a random sampling method, so the radius is required to be long enough to ensure the accuracy and stability of the field surveyed LCCs. As is shown in the left of Fig. 5, when the radius is small (2 m to 4 m), the variation of the field surveyed local LCCs estimated using radii of 2 m and 4 m appear very large, whereas the differences become small between the field surveyed local LCCs calculated using radii of 28 m and 30 m. The fact that the variation of the field surveyed local LCCs decreases with the increase of the radius can also obviously be seen in the right of Fig. 5, where the variation for a radius of R is calculated by the following equation:

$$Variation(R)=\frac{1}{N(\mathbf{P})}\sum_{p\in\mathbf{P}}[LCC_p(R+1)-LCC_p(R-1)]^2 \tag{15}$$

where R is the selected radius for the local LCC measurement, p is the position to calculate the variation of the field surveyed local LCCs, $\mathbf{P}$ is the set consisting of all p along a specific transect, and $N(\mathbf{P})$ is the number of positions, so $LCC_p(R+1)$ and $LCC_p(R-1)$ represent the field surveyed local LCCs at position p of the ruler, which are calculated by using radii of $R+1$ and $R-1$, respectively.

Optics EXPRESS

As illustrated on the right in Fig. 5, to make sure the field surveyed LCCs are stable enough, the radius needs to be at least 25 m. This is also the reason why the increments of the correlation coefficients become micro once the radii reaches approximately 25 m for the ZY-3 and WV-3 images, as shown in Fig. 4.

In summary, to make sure the field surveyed LCCs are accurate and stable, the selected radius needs to be longer than approximately 25 m. As the length of the surveyed transects is only approximately 100 m, the radius is unable to select a very long length, i.e. choosing in the range of 25—40 m should be proper.

In the remaining experiments, the field surveyed local LCCs around Weizhou Island are calculated by the method described in Appendix A with the radius of 35 m, where the radius is just longer than 25 m and shorter than 40 m.

3.2 Estimation of the LCCs and accuracy assessment for Weizhou Island

Once the radius for calculating the field surveyed local LCCs is determined, we can then further apply the methods proposed in section 2.3 to the experimental images. The results are shown in Fig. 6. Except for a few local regions, the distributions of the LCCs estimated from different images are seen to be overall similar to each other.

The valid region of the ZY-3 image appear to be much wider than the WV-3 image. The reason is that the water captured by the ZY-3 image is clearer than the WV-3 image. For example, according to our calculation, the mean of the diffuse attenuation coefficient of the blue band of the ZY-3 image is 0.0371, while the mean of the diffuse attenuation coefficient of the blue band of the WV-3 image is 0.0529.

According to Khanna et al. [54] and Longbotham et al. [37], WV-3 images may have SNR comparable to airborne visible infrared imaging spectrometer (AVIRIS), while Rutherford and Alexander [55] pointed out that the average SNR of AVIRIS data can be 5.5 to 13 times as large as Landsat ETM + images under typical signal radiance. Since the SNR of the Landsat ETM + images ranges from 30 to 40 (https://landsat.usgs.gov/), we conclude that the SNR of the WV-3 image is approximately 170—520. Such SNR is larger than those of the ZY-3 image (40—50). Besides, there are also obviously gaps between the wavebands of the ZY-3 and the WV-3 images, e.g. the green band of the ZY-3 image ranges in 520—590 nm, but corresponding band of the WV-3 image ranges in 510—580 nm. Hence the local LCC differences between the ZY-3 and WV-3 images may be partly caused by those different SNR or wavebands.

More likely, the local LCC differences are mainly caused by the different ground resolution of the two experimental images. According to the work of Zhao et al. [56], there is about 15% of the LCC differences between the 1 m^2 photo-quadrat and the near 10 m line transect being larger than 10; and Zhang et al. [57] also reported that the LCC differences between 20 m line intercept transect and 50 m video transect range from 0.15 to 10.51. Although such differences can be ignored in practical ecological investigation of coral reefs as mentioned in Appendix A, such phenomenon indicates that a few of the LCC differences caused by different ground resolution can likely reach 10 or more. Thus, different ground resolution can likely be the main reason for the local LCC differences between the ZY-3 and WV-3 images, as the ground resolution of the ZY-3 and WV-3 images are 5.8 m and 1.24 m respectively.

Optics EXPRESS

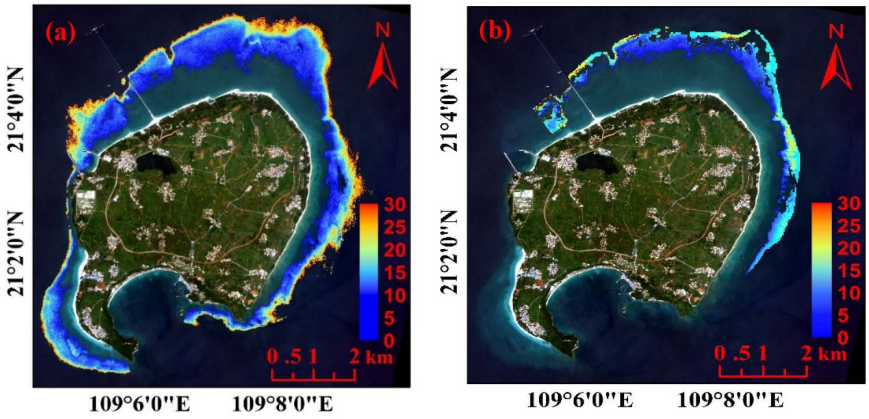

Fig. 6. The LCCs estimated by the constructed RDLCs: (a) LCCs estimated from the ZY-3 image; (b) LCCs estimated from the WV-3 image.

As seen in Fig. 6, most of the LCCs are less than 30, but the distribution of the live corals can still be clearly seen in figure: the live corals are mainly distributed around the east, the north, and the northwest of Weizhou Island, while the LCC of the southwest is obviously less than the east, the north, and the northwest.

To further assess the accuracy, we compare the estimated LCCs with the field surveyed ones as shown in Fig. 7. The field surveyed LCCs were obtained by using their reserved half, as described in Appendix A.

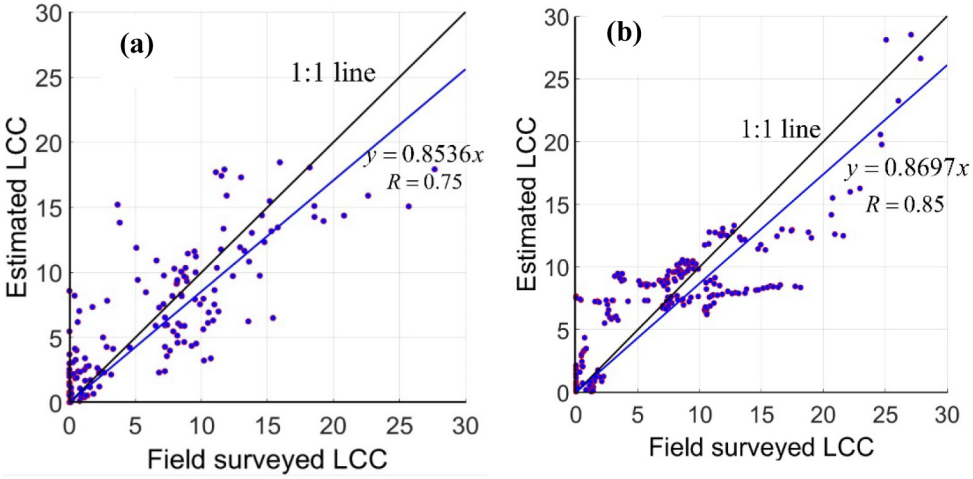

Fig. 7. The comparisons between the estimated LCCs and the corresponding field surveyed ones for the constructed RDLC indices: (a) the comparisons for the ZY-3 image; (b) the comparisons for the WV-3 image.

Optics EXPRESS

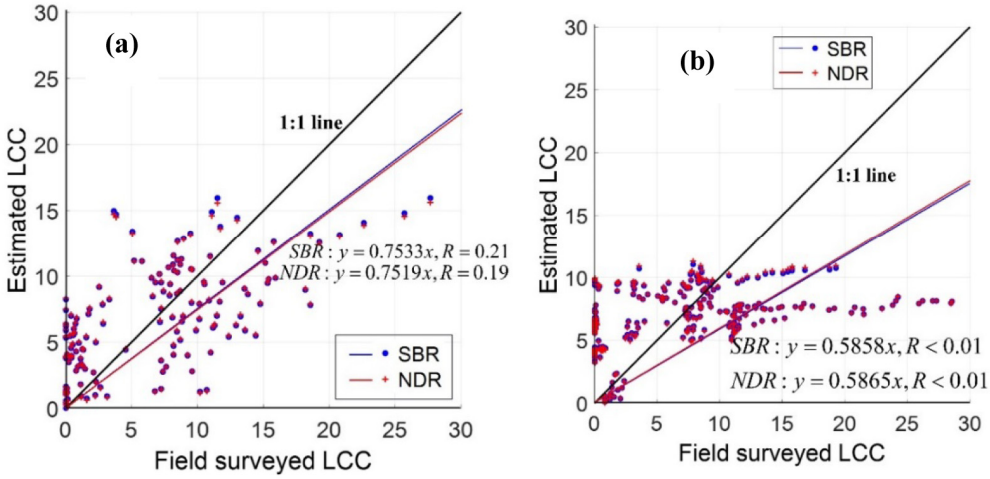

Fig. 8. The comparisons between the estimated LCCs and their corresponding field surveyed ones for SBR and NDR: (a) the comparisons for the ZY-3 image; (b) the comparisons for the WV-3 image.

Although we can observe the comparisons from Fig. 7 intuitively, the improvement of the constructed RDLC indices is difficult to derive from the figure. Since RDLC is extended from SBR and NDR, we further compare the results with those of SBR and NDR.

Some studies [9, 11, 24, 26] illustrated that SBR or NDR of 529:439 nm (Green-Coastal bands) showed the greatest sensitivity to the LCC variations around clear-water reefs. Thus, we select for testing the SBR and NDR of Green-Coastal bands for the WV-3 image. As there is no Coastal band for the ZY-3 image, hence the Green-Red bands is used instead of Green-Coastal bands for testing the results of the ZY-3 image. The reason is that the NDRs of the Green-Red bands have proven to be the highest correlation to the field surveyed LCCs among the NDR combinations without a Coastal band. The results of these comparisons are shown in Fig. 8.

Table 1. Statistics of the LCCs for the SBR and NDR indices for the field surveyed local LCCs.

Image	Index[a]	CC[b]	RMS[c]	P-value	RMSE[e]	MRE[d]
ZY-3	RDLC	0.824	3.54	< 0.001	3.52	28.3%
	SBR	0.660	4.66	< 0.001	4.61	45.2%
	NDR	0.658	4.67	< 0.001	4.62	46.1%
WV-3	RDLC	0.856	3.38	< 0.001	3.65	23.2%
	SBR	0.455	5.87	< 0.001	5.95	55.5%
	NDR	0.456	5.86	< 0.001	5.95	54.9%

[a]RDLC is the proposed RDLC index in this paper, SBR and NDR are the simple band ratio and the normalized difference ratio described by Collin et al. [26], and they are calculated using the Green and Red bands for the ZY-3 image, and the Green and Coastal bands for the WV-3; [b]The correlation coefficient between index values and the field surveyed LCCs; [c]The root mean square of the residuals for the regression of Eq. (8) (for SBR and NDR, SBR and NDR indices are used instead of RDLC); [d]The mean relative error estimated by the method illustrated in Appendix B; [e]The root mean square error calculated by Eq. (16).

Besides, to show the accuracies more clearly, corresponding quantitative statistics of those comparisons are further summarized by Table 1. Note that the root mean square errors (RMSEs) in the table are calculated with the following equation:

$$RMSE = \sqrt{\frac{1}{N}\sum_{i=1}^{N}(LCC_{f,i} - LCC_{e,i})^2} \tag{16}$$

where N is the number of the estimated LCCs, $LCC_{e,i}$ is the i-th estimated local LCC, and $LCC_{f,i}$ is the corresponding i-th field surveyed local LCC.

As shown in Fig. 8, there is no significant difference between SBR and NDR for the experimental images, and this is also quantitatively verified by the statistics of Table 1. However, it is seen from Fig. 8 that the errors for SBR and NDR are both large, as the LCCs estimated by both SBR and NDR obviously deviate from the field surveyed ones. As shown in Table 1, the RMSEs of SBR and NDR range from 4.6—6.0, and the MREs even reach approximately 45—56%. In fact, this is the direct motive for us to develop the RDLC index.

When Fig. 7 is compared with Fig. 8, great improvements are found for the constructed RDLC indices. These improvements are further quantitatively demonstrated by Table 1: the correlation coefficients (CCs) increase from 0.45 to 0.67 for SBRs and NDRs to 0.82–0.86 for the constructed RDLCs, while the root mean square errors (RMSEs) and the mean relative errors (MREs) are reduced from 4.6 to 6.0 and 45–56% for the SBRs and NDRs to 3.5–3.7 and 23–29% for RDLCs, respectively. Such results not only verify the effectiveness and feasibility of the constructed RDLC indices for Weizhou Island but also illustrate great improvement in accuracy when comparing the constructed RDLCs with SBRs and NDRs.

Note that the correlations between SBRs (NDRs) and the LCCs are usually derived by using hyperspectral data and simulation, or tested on very clear-water environments [9, 11, 24–26]. However, seawater around Weizhou Island seems not to be the clearest, and it has a transparency of only 3.0—10.0 m [31]. Meanwhile, multispectral satellite images are different from hyperspectral data, e.g., multispectral images usually have much wider bandwidths than those of hyperspectral data. What is worse, LCCs around Weizhou Island are not greater than 30% according to our field measurement. In other words, the radiances recorded by the multispectral images are mixed signals of different substrates. This spectral mixing problem should be one of the greatest differences between the experimental images and those of previous studies. As a result, the synthetic effect of these three factors may be the reason why the errors of the LCCs estimated by SBR and NDR are seen to be larger in the experiments.

On the other hand, the constructed RDLC indices consist of various linear combinations of water depth and different wavebands in the numerator and denominator. The proposed method for estimating the parameters further makes sure the final constructed RDLCs correlate most to the field surveyed LCCs. Such models may eliminate the influence of the water column and provide the most LCC-sensitive indices. We think this is one of the reasons why the constructed RDLC indices are able to greatly improve the accuracy of the estimated LCCs in contrast to both SBR and NDR for Weizhou Island.

3.3 Experimental results for Palmyra Atoll

Palmyra Atoll data is introduced to our experiments for further testing the proposed RDLC index in a second validation site. Since the LCCs of the Palmyra Atoll data is provided by only four live coral density classes (0–10, 10–50, 50–90, and 90–100), the implementation was modified as described in at the end of section 2.2.3.

As illustrated by the modified implementation, 5600 points were randomly selected from the Palmyra Atoll data, where one half is used as training data, and the other half is used as check data. To clearly shown the checking, we count the percent of the check errors that range in different error intervals, as shown in Fig. 9. Those check errors are calculated by using Eq. (12) with the trained parameters.

Optics EXPRESS

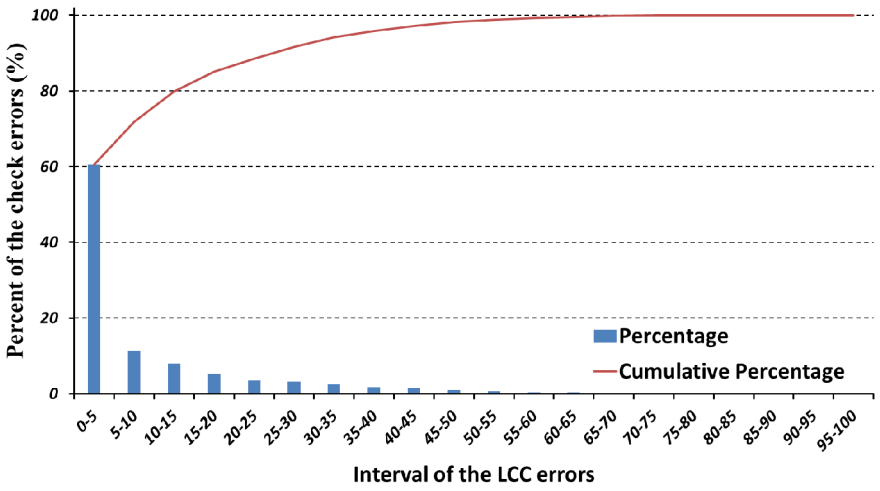

Fig. 9. Statistics of the check errors for the RDLC index (Palmyra Atoll, EO-1 ALI image).

As seen in Fig. 9, for the EO-1 ALI image, 61% of the LCC errors are lower than 5, 71% are less than 10, while 80% are not greater than 15. Note further that the EO-1 ALI image has a ground resolution of only 30 m, which is 12 times lower than Quickbird-2 and 7.5 times lower than IKONOS. However, when OBIA was applied to 2.4 m resolution Quickbird-2 and 4.0 m resolution IKONOS satellite images by Phinn et al. [14, 15], the overall accuracy of 'benthic community' classifications was found ranged in 52% to 75%. As a result, the RDLC should be thought being also effectiveness when it is applied to the EO-1 ALI image of the Palmyra Atoll. Besides, another advantage is that such RDLC approach means a possible away to estimate continuous LCC values even if the training data is based on several levels of coral density.

As previously mentioned, EO-1 ALI was used to test the OLI on Landsat 8, so the RDLC can now be concluded to be effective for some other freely available images (e.g. OLI) with a degree of certainty too. In fact, we have also applied an OLI image captured on October 23, 2015 to the field surveyed LCC data around Weizhou Island. The ground resolution of the OLI image is 30 m, which is much lower than ZY-3 and WV-3 images. As a result, the number of field surveyed local LCCs derived by the methods described by Appendix A is much less than those of the ZY-3 and WV-3 images (only a total 33 LCCs for the OLI image), so there is almost no redundancy in the training approach. Nevertheless, the final result can still show that the RMSE and MRE can reduced from 3.1 and 65% to about 2.6 and 22%. This can enhanced the conclusion that the proposed RDLC is also feasible for OLI images.

3.4 Supplementary notes and future work

One of the most significant aspects of the study is to provide a new train of thought for designing RDLCs for LCC estimation, followed by corresponding solutions. Experimental results have demonstrated that the proposed method is effective and feasible for the two different experimental sites with several different types of multispectral images. However, the following two aspects are still not fully resolved in the study:

(1) For simplification, we introduce the process pattern of empirical band combination bathymetric methods to see a_i, a_i', b, b', c, and c' as independent variants of the constructed RDLC indices, but this process pattern may cause the physical meanings of the parameters to be changed or lost;

(2) Some parameters, such as b, b', c, and c', depend on the properties of the atmosphere and the water column, the geometric factor of the path-length through the water, and the solar irradiance, etc. The consequence is that they should be re-estimated for individual images using the appropriate field surveyed LCCs.

As a consequence, the proposed RDLC method still require the described training validation step for a new reef or a new sensor. Hence future work should focus mainly on how to solve the two problems so as to make the proposed RDLC method being independent of field surveyed LCC data and application sites. Fortunately, Eqs. (7)–(10) have already indicated possible thinking to solve such problems. Specifically, Eqs. (7) and (8) show that the parameters a_i, and a_i' of the constructed RDLCs and the parameters m and n of the regression are independent of environmental parameters (the properties of the atmosphere and the water column, the geometric factor, and the solar irradiance, and so on), so they are possible to estimate independently using simulation methods and plenty of field surveyed substrate spectrum data. Thereafter, the remaining parameters b, b', c, and c' can be estimated by using the effective diffuse attenuation coefficient of the water column $\kappa(\lambda)$, the geometric factor of the path-length through the water f, and $t(\lambda)$, which is dependent on the solar irradiance, the transmittance of the atmosphere and water surface, and the reduction of the radiance due to refraction at the water surface. Inspired by Lee et al. [44], Eugenio et al. [58], and Huang et al. [35], $\kappa(\lambda)$, f, and $t(\lambda)$ may be estimated with semi-analytic methods on the multispectral images themselves that do not require any field surveyed data.

For this reason, we plan to work on expressions of $\kappa(\lambda)$, f, and $t(\lambda)$ to fit the utilized radiative transfer model (Eq. (1)), and simulations on field surveyed substrate spectrum data to obtain more general a_i, a_i', m, and n in the future. The purpose is to make the training step being independent of application sites, sensors, and field surveyed LCCs, or let the proposed RDLC method become more generalizable.

4. Conclusions

In this paper, SBR and NDR are extended to an entirely new index defined as RDLC for estimating the LCCs from multispectral satellite images. On the basis of field surveyed LCCs, an empirical process pattern inspired by the solution of band combination bathymetric methods is also proposed to determine the parameter values of the RDLC. The effectiveness and feasibility have already been verified by our experiments on the ZY-3 and WV-3 multispectral images of Weizhou Island: the MREs are reduced from 45 to 56% for SBRs and NDRs to 23–29% for the constructed RDLCs, while the RMSEs improved from 4.6 to 6.0 for SBRs and NDRs to 3.5–3.7 for the RDLCs. Finally, the effectiveness of the proposed RDLC is further enhanced by the experiment on an EO-1 ALI image of a second site (Palmyra Atoll).

What is more, the proposed method has actually provided novel thinking for designing RDLC indices for LCC estimation from given multispectral images. Following this thinking, more general process methods for solving the RDLC parameters have also been noted during the experiments, and it is possible to let the solution of the RDLC be independent of field surveyed LCCs and application sites. If so, the parameters of the RDLC can be then re-estimated individually for any other image without field surveyed LCC data, which will become our main focus in the future.

Appendix A. Field surveyed LCC data around Weizhou Island

We investigated the LCCs of Weizhou Island in October 2015 using the video line intercept transect technique [8, 10, 56, 57]. According to the work of Zhang et al. [57], the most commonly used line intercept transect [8, 56] can be replaced by video line intercept transect in LCC monitoring, because the deviations of the LCCs were only 0.77—6.11 between the

Optics EXPRESS

line intercept transect and the video transect, and only 0.08 for the average value. Meanwhile, Zhao et al. [56] further indicated that most of the LCC differences between the 1 m^2 photo-quadrat and the near 10 m line transect range from 0.15—9.31, while the average is only 0.26. As a result, Zhao et al. [56] declared that the LCC result of line intercept transect, video line intercept transect, and photo-quadrat was similar to each other enough for coral reef ecological investigation. Another reason for us to choose the video line intercept transect technique is that video line intercept transect has advantages of saving diving time, providing permanent record, and no need for life-form identification in field.

Specifically, thirteen transects were visited at different positions around Weizhou Island, as shown in Fig. 10. For each transect, one 100-m measuring ruler was fixed to the sea floor between the starting and ending points, and then a scuba observer used an underwater Olympus TG-2 camera to record videos along the transect, as shown in Fig. 11. Meanwhile, the starting and ending points of the survey transects were labelled with two flag floats, so the horizontal geography positions were mapped by a Magellan eXplorist 610 hand-held GPS navigation instrument with an accuracy of 3 m.

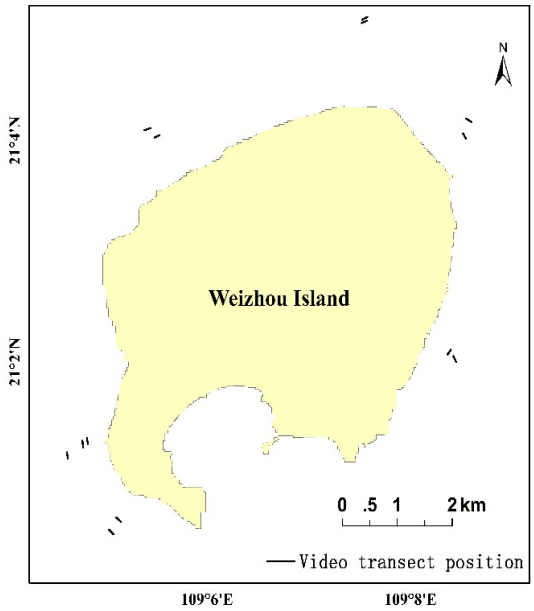

Fig. 10. The position distribution of the video transects around Weizhou Island.

Optics EXPRESS

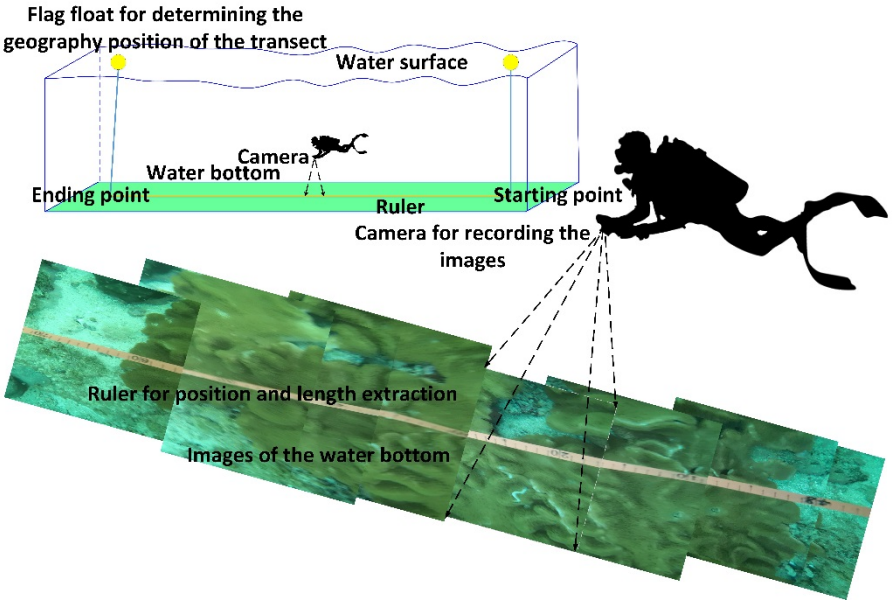

Fig. 11. The method of recording the transect video for field LCC estimation.

Thereafter, the live corals along these transects were manually interpreted from the video images, as well as their positions and lengths according to the ruler, as shown in Fig. 12. Accordingly, the local LCC at each point of these transects was then calculated by using the method shown in Fig. 13. Note that LCCs are usually expressed by percentages to show the proportion of live corals in the water bottom.

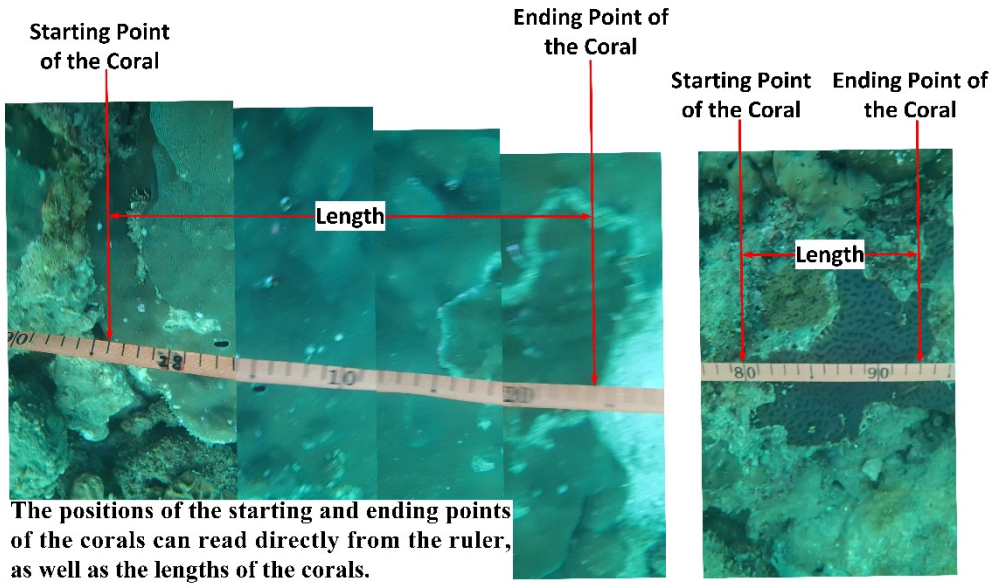

Fig. 12. The method for reading the position and length of live corals along the video transect.

Optics EXPRESS

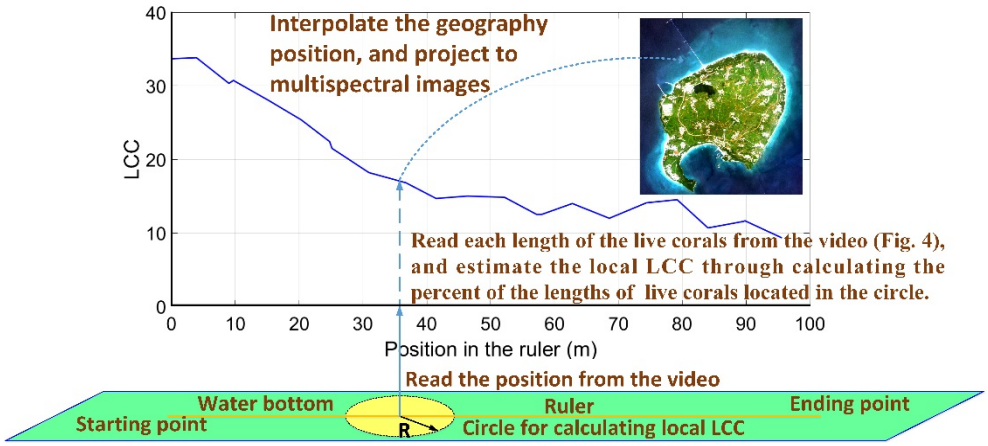

Fig. 13. The estimation of field surveyed LCCs and their matching to multispectral images: for such an approach, we can assign several pixels with LCCs for a specific transect.

As we can estimate the geographic position of each point for these transects using linear interpolation according to the mapped geography positions of the starting and ending points, the calculated LCCs can be finally matched to satellite data by using the interpolated geography positions and the geo-referenced information of the multispectral images. In other words, we can assign a local LCC to each pixel along those transects projected into the multispectral images.

Appendix B. Methods for estimating the mean relative error (MRE)

To estimate the MREs for the experiments, we analyse Fig. 7 and Fig. 8 in detail. First, the abscissa and ordinate of these figures represent the field surveyed LCCs and the estimated LCCs. For any individual point **P** in the figure, we assign the coordinates (C_f, C_e), as shown in Fig. 14. The line connecting the point to the origin can be expressed by the following equation:

$$y = kx \tag{17}$$

Optics EXPRESS

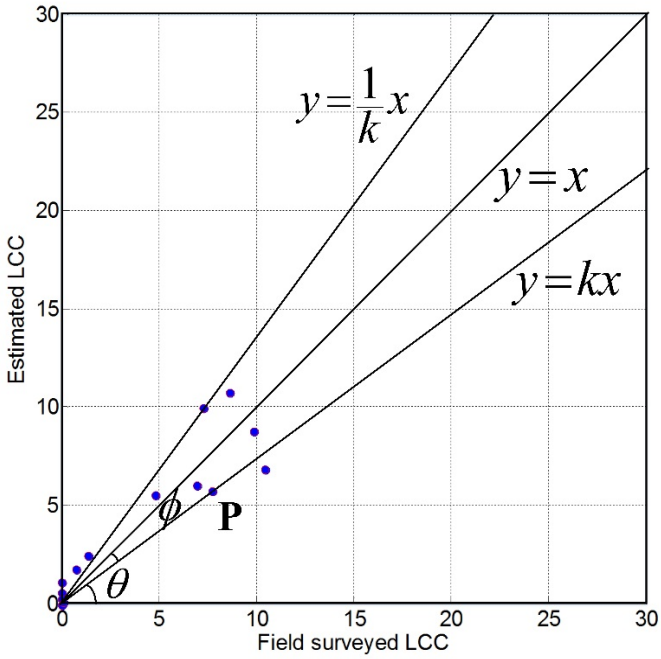

Fig. 14. Diagram for MRE estimation

As seen in Fig. 14, k can be expressed by

$$k = \tan\theta \tag{18}$$

where θ is the angle between the abscissa and the line connecting point **P** to the origin. As a result,

$$\tan\phi = \tan(45^\circ - \theta) = \frac{1-\tan\theta}{1+\tan\theta} = \frac{1-k}{1+k} \tag{19}$$

On the other hand, k can also be expressed by

$$k = \frac{C_e}{C_f} \tag{20}$$

Substituting Eq. (20) into Eq. (19), we can obtain

$$\tan\phi = \frac{C_f - C_e}{C_f + C_e} \tag{21}$$

Obviously, the numerator represents the error of the LCC value, whereas the denominator is approximately equal to two times of the LCC value. Hence, the relative error (RE) can be estimated by using the following expression:

$$RE = 2\tan\phi = 2\frac{1-k}{1+k} \tag{22}$$

In other words, we can estimate RE through calculating k.

Note that the symmetrical line of $y = kx$ about $y = x$ can be expressed by

Optics EXPRESS

$$y = \frac{1}{k}x \tag{23}$$

The cone formed by $y = kx$ and $y = \frac{1}{k}x$ shown in Fig. 14 can then be seen as a geometric figure describing the RE of the LCC.

Accordingly, to further estimates of the MRE, we calculate the average k through the following approach:

(1) For any $\mathbf{P}_i = (C_{fi}, C_{ei})$, we calculate its minimum distance to the cone formed by $y = kx$ and $y = \frac{1}{k}x$ as follows,

$$d_i = \min\left\{ \left| \frac{C_{ei} - kC_{fi}}{\sqrt{1+k^2}} \right|, \left| \frac{kC_{ei} - C_{fi}}{\sqrt{1+k^2}} \right| \right\} \tag{24}$$

(2) Thereafter, we can then construct the following objective function,

$$L(k) = \sum\nolimits_i d_i^2 \tag{25}$$

(3) Finally, the optimal k is searched using the Genetic Algorithm (GA) tool of Matlab 2012b software to minimize this objective function. This optimal k is assigned as $\bar{k}$ and used as the average of k.

Now, the MRE can be then estimated by substituting $\bar{k}$ into Eq. (22) as follows:

$$MRE = 2\frac{1-\bar{k}}{1+\bar{k}} \tag{26}$$

Funding

Natural Sciences Foundation of China (91428203, 41766007); Science and Technology Project of Guangxi (AD17129063); BaGui Scholars Program Foundation (2014BGXZGX03); Natural Sciences Foundation of Guangxi, China (2016GXNSFBA380031).

Acknowledgments

We are very grateful to our colleagues, Dr. Kun Hu for their precious comments and revision of the language, and special thanks are given to the anonymous reviewers and members of the editorial board for their suggestions of improving this article.

Disclosures

The authors declare that there are no conflicts of interest related to this article.